Noname manuscript No.
(will be inserted by the editor)

A new atmospheric-like differentially heated rotating annulus configuration to study gravity wave emission from jets and fronts.

Costanza Rodda · Steffen Hien · Ulrich Achatz · Uwe Harlander

Received: date / Accepted: date

Abstract Significant inertia-gravity wave activity has been frequently observed in the vicinity of jet and front systems in the atmosphere. Although many studies have established the importance of these non-orographic sources, the mechanisms responsible for spontaneous wave emissions are still not fully understood. The complexity of the three-dimensional flow pattern and distribution of the sources over large areas point towards the need for laboratory experiments and idealised numerical simulations. These will help understand the correct interpretation of the fundamental dynamical processes in a simplified, but yet realistic flow. In this study, we emphasise the importance of using setups of the differentially heated rotating annulus experiment with a ratio between the buoyancy frequency N, and the Coriolis parameter f larger than one to investigate atmosphere-like emission of gravity waves from baroclinic jets. Indeed, in the atmosphere $N/f \sim 100$, but for table-top size experiments this ratio is smaller than one, resulting in an unfavourable condition for the propagation of gravity waves. For this reason, we offer a newly built laboratory experiment supported by numerical simulations that allow $N/f > 1$. The conditions for gravity wave emission in this new configuration are examined in detail, and the first evidence of IGWs is reported. Moreover, we compare numerical simulations and experimental data focusing on the variations of the temperature T, and its effects on the buoyancy frequency N. It becomes clear, that despite the fact the global structure and baroclinic instability characteristics are very similar, the model and experiment show deviations in N with implications for gravity wave emission. Due to the complex horizontal structure of N, where the largest values occur along the baroclinic jet axis, the inertia-gravity waves in the experiment are observed to be trapped.

Keywords Thermally driven rotating annulus · Gravity waves · Baroclinic waves

1 Introduction

The differentially heated rotating annulus is a classical laboratory experiment widely used to study the dynamics of rotating, stratified flows. Extensive research has proven the capability of this experiment to reproduce the main features of the global and synoptic scale motions in the atmosphere, namely the large-scale circulation and the baroclinic waves (Read et al., 2014). The experiment was even used to test atmospheric data assimilation methods (Young and Read, 2013). However, in recent years, the focus has shifted to small-scale phenomena such as inertia-gravity waves (IGWs) both in numerical simulations (Jacoby et al., 2011; Randriamampianina and del Arco, 2015; Von Larcher et al., 2018; Hien et al., 2018) and laboratory experiments (Vincze et al., 2016; Rodda et al., 2018). IGWs, which are observed ubiquitously in the atmosphere playing

This work was supported by the Spontaneous Imbalance project (HA 2932/8-1 and HA 2932/8-2) that is part of the research group Multiscale Dynamics of Gravity Waves funded by DFG (FOR1898).

C. Rodda · U. Harlander
Department of Aerodynamics and Fluid Mechanics, Brandenburg University of Technology Cottbus-Senftenberg, Siemens-Halske-Ring 14, 03046 Cottbus, DE
E-mail: rodda@b-tu.de

S.Hien · U. Achatz
Institute for Atmospheric and Environmental Sciences, Goethe University Frankfurt, Altenhöferhallee 1, 60438 Frankfurt am Main, DE

an essential role in the vertical transport of momentum, can have scales smaller than the current resolution of the climate models. For this reason, they need to be parametrised. Despite recent efforts to investigate IGW properties and their generation mechanisms, some aspects remain poorly understood. Among these are gravity wave radiation processes from non-orographic sources, especially jets and fronts (Plougonven and Zhang, 2014). These processes have been studied in the shear-driven version of the rotating annulus, where IGWs have been observed in the vicinity of the baroclinic jet by Lovegrove et al. (2000) and Williams et al. (2005). This experimental set-up differs from the differentially heated rotating annulus because the tank is filled with two immiscible fluids, and the baroclinic instability is driven by the vertical shear created mechanically with a differentially rotating lid. With the help of a numerical model of the annulus, the generation mechanism of the observed gravity waves has been investigated and identified as spontaneous generation by Williams et al. (2008). A modified version of this two-layer experiment has been proposed in Flór et al. (2011), where they used a salty stratified fluid instead of two fluids of different density. Part of the small-scale waves observed in this configuration is claimed to be generated by the Hölmböe instability occurring at the density interface. In a successive investigation of the same experiment done by Scolan et al. (2014), it emerged that the origin of the small-scale waves could not be entirely explained by linear shear instability and the possible mechanisms proposed for the radiation of IGWs are spontaneous emission or Rossby-Kelvin instability.

Despite the observations in several experimental configurations, spontaneously emitted gravity waves have not been observed experimentally yet in the differentially heated rotating annulus with a radius in the order of 10 cm filled with a constant density fluid. This configuration, to which we will refer to as "classical" set-up, is often used in the laboratories (Hide and Fowlis, 1965; Ukaji and Tamaki, 1989; Früh and Read, 1997; Von Larcher and Egbers, 2005). We identify the cause for this lack of observations in the unusual, in meteorological terms, ratio between the buoyancy frequency N and the Coriolis frequency f smaller than 1. Because this ratio is much greater than one in the atmosphere, it can be expected that IGW properties—which depend on N and f according to their dispersion relation—differ between experiment and atmosphere. For $N/f < 1$ waves can still propagate in the flow, but they are inertial waves, which are rotation dominated, and differ from gravity waves in several aspects. Since we aim to study atmospheric jet generated waves, which are gravity dominated, to obtain similar features it is fundamental to use configurations of the experiment that allow $N/f > 1$. Such configurations can be achieved either increasing N directly by introducing density stratification (Rodda et al., 2018), or by reducing the aspect ratio Π between the total fluid depth H and the fluid gap L. The latter solution, to which the present study is dedicated, leads to $N/f > 1$ for a small Burger number that allows to remain in the baroclinically unstable regime.

Several studies (Hide and Fowlis, 1965; Lambert and Snyder, 1966; Douglas and Mason, 1973) investigated the effects of changing the aspect ratio on the flow regime in a differentially heated rotating annulus. They found that the stability curve, which determines when baroclinic instability can occur, is affected by the parameter Π. What emerges from these studies is that in configurations with a tall annulus, the Ekman layer is small compared to the total fluid depth and the large-scale flow is not affected by Ekman friction. When the fluid depth is decreased for heating and rotation kept constant, on the other hand, friction becomes more and more dominant and can, therefore, no longer be neglected.

The purpose of the present study is to demonstrate that a baroclinic wave experiment with a working fluid of homogeneous density needs a small Π to reach $N/f > 1$. However, to avoid ending up in an Ekman dominated flow, H must be in the order of at least a few centimetres. This, in turn, implicates an L in the order of decimetres.

In the first part of this paper, we search for the critical fluid depth that barely allows for regular baroclinic waves. We do this first by looking at simple heuristic arguments that use solutions from the theoretical model by Eady (1949), and then confirm those with experimental results. We do our analysis for a free surface, i.e. comparing free surface data with the free surface model by O'Neil (1969). Such a comparison has, to the best knowledge of the authors, never been done before. In the second part, we go into more detail and present the spatio-temporal patterns of N/f and the signature of gravity waves occurring in regions of the flow where the local Rossby number is large for a newly built rotating annulus with a more atmosphere-like configuration. The construction of this experiment follows the arguments we have given in the first part of this study and the configuration was firstly suggested by Borchert et al. (2014). Their numerical studies—using such a configuration with a wider gap, shallower flow, and a large radial temperature contrast—lead to the identification of spontaneously emitted IGWs (Borchert et al., 2014; Hien et al., 2018). In the conclusion of the paper, we

briefly comment on the consequences of the rather complex N/f field for IGW radiation and propagation in the newly designed experiment.

2 Transition curves for shallow water set-up

2.1 Inviscid systems and geometry effects

One of the first mathematical models to explain the baroclinic instability mechanism was developed in the late 1940s by Eady (1949). This inviscid theory consists of a linear stability analysis of the mean flow for a quasi-geostrophic fluid in a vertically bounded rotating domain with superposed small perturbations. The mode is found to be stable whenever the Burger number, Bu, satisfies

$$Bu = \frac{Hg\alpha\Delta_z T}{4\Omega^2(b-a)^2} \geq \frac{0.581}{\left(l^2 + \frac{m^2}{\pi^2}\right)}, \tag{1}$$

where m is the azimuthal and l is the radial wavenumber, g is gravity, and α the thermal expansion coefficient (Drazin, 1978). The values of the parameters are given in table 2. Bu is a dimensionless number, written here in terms of the parameters of the differentially heated laboratory experiment, and $\Delta_z T$, which is related to the internally determined vertical temperature gradient $\partial T/\partial z$ multiplied by the total fluid depth H. Note that in the laboratory experiment the upper boundary condition is free surface while the Eady model uses a rigid boundary. If friction can be neglected and one assumes that surface waves do not affect the baroclinic waves, then a free upper surface and a rigid lid are equivalent, at least for the baroclinic wave dynamics as experimentally shown by Fein (1973).

When studying rotating fluids, another useful dimensionless number—defining the ratio between inertial and Coriolis forces—is the Rossby number $Ro_T = U_T/(fL)$, where U_T is the typical velocity scale, $f = 2\Omega$ is the Coriolis parameter, and the gap width $L = (b-a)$ defines the horizontal dimension. For the flow in the rotating annulus, the fluid velocity is given by the thermal wind equation $U_T = (Hg\alpha\Delta T)/(fL)$, where $\Delta T = (T_b - T_a)$ is the externally impressed radial difference of temperature (with T_b the temperature at the outer warm wall and T_a the temperature at the inner cold wall). By substituting U_T into the definition of Ro_T, we have

$$Ro_T = \frac{Hg\alpha\Delta T}{4\Omega^2(b-a)^2}, \quad Bu = \sigma_z Ro_T. \tag{2}$$

Note that a universal definition of the thermal Rossby number is lacking and some authors define it with Ω instead of f in the denominator; a factor 4 might, therefore, be needed to compare data from different sources. Following Hide (1967), we define the dimensionless parameters $\sigma_z = \Delta_z T/\Delta T$ and $\sigma_r = \Delta_r T/\Delta T$, where $\Delta_r T = (b-a)\partial T/\partial r$ is the radial temperature gradient in the fluid interior multiplied by the horizontal dimension of the annular gap. The Burger number is, therefore, proportional to the thermal Rossby number multiplied by σ_z, corresponding to the mean slope of the isotherms. It can immediately be seen that, under the assumption that $\Delta_z T \approx \Delta T$ (we shall discuss the validity of this assumption in section 3.1), the Burger and the thermal Rossby number are equivalent. Another consequence of making this assumption is that the buoyancy frequency, which depends on the stratification of the fluid, can be written as $N^2 = g\alpha\Delta T/H$. In this way, the Burger number can be rewritten as

$$Bu = \left(\frac{N}{f}\right)^2 \left(\frac{H}{L}\right)^2. \tag{3}$$

Shallower systems have a greater value of N for baroclinic waves, given the same imposed radial temperature difference. It can, therefore, be seen how the geometry of the rotating annulus becomes crucial when using it for the study of inertia-gravity waves, the frequencies of which strongly depend upon N. A similar argumentation about the importance of geometry in numerical simulations has been discussed by Borchert et al. (2014).

One of the generation mechanisms of inertia-gravity waves still not fully understood is spontaneous emission. Although spontaneous emission in stratified fluids could not be reduced to a single process yet, it is however frequently connected to spontaneous emission in rotating shallow-water (RSW) flow. For RSW it can be related to Lighthill radiation, where the source is considered to be small compared to the emitted long waves and it is assumed that the Rossby number is $Ro > 1$ and the Froude number $Fr = U/(gH)^{1/2} << 1$ (Vanneste, 2013; Sugimoto et al., 2008). Lighthill radiation of gravity waves is based on the isomorphism between compressible waves and shallow water surface waves. Studying baroclinic waves in a continuously stratified fluid, as we do in the differentially heated rotating annulus, this isomorphism breaks down but spontaneous gravity wave emission is still possible, although it differs from Lighthill radiation. Since in stratified flows $Fr = U/(NH)$, and hence $Bu = (Ro/Fr)^2$, we find that in flow regimes with $\Delta_z T \approx \Delta T$ the Froude number depends on the thermal Rossby number via $Fr \approx Ro^{1/2}$. This implies that in stratified flows the background condition typical for the RSW Lighthill

radiation cannot be reached if the vertical temperature difference equals the lateral temperature difference. Therefore, it is not yet clear at which region in the $Ro - Fr$-space we can expect the most effective gravity wave radiation.

Figure 1(a) shows, for fixed $Bu = 0.6$ (i.e. where the onset of baroclinic instability is predicted by the Eady model, according to (1)) and $Fr = 0.77$, the variation of N as a function of the rotation rate Ω, calculated with (3) for different experimental set-ups tested in the laboratories at BTU. The label "small-tank" refers to the classical set-up (see the second column in table 2 for more details) with maximum and minimum fluid depths. The label "big-tank" refers, instead, to the new experiment (see the third column in table 2 and section 3) with characteristics more similar to the atmosphere. For comparison, a thermohaline configuration of the small-tank experiment is also shown in the plot and labelled as "barostrat" (see Rodda et al. (2018)). This experiment, for which $N/f > 1$ is reached by introducing a vertical salinity gradient, represents a special case since the baroclinically unstable layer lies on top of a stably stratified layer. For this reason, it has no bottom Ekman layer influencing the flow. Rodda et al. (2018) observed inertia-gravity waves trapped along the baroclinic jet and showed that barostrat is, for some aspects, an ideal experiment to study emission and propagation because of the formation of alternating baroclinically unstable and stable layers, qualitatively resembling the troposphere and stratosphere. The latter is too stably stratified for baroclinic instability.

As it can be seen in figure 1(a), the black line for the small tank with a fluid depth of $z = 13.5\,\mathrm{cm}$ is below the line $N/f = 1$ (in purple) whereas the red line for the atmosphere-like big tank is above that curve. For this reason, with the big tank we are closer to the atmospheric case since $f < \omega < N$. Note that we have $N/f \approx 2$ which is still small compared to the atmosphere where $N/f = 100$. It is, moreover, relevant to point out that for typical laboratory conditions, which give $N \approx 0.5$ rad/s, the big tank rotates much slower in comparison to the small tank. By reducing the water depth in the small tank to $z = 3$ cm, which is the shallowest configuration for which a regular baroclinic wave was observed (see section 2.2 figure 3), N/f raises to 1.2; however this is, in fact, an unfortunate configuration for investigating IGWs since the frequency band for this case is rather narrow. Finally we mention that, for the barostrat experiment, N/f in the baroclinically unstable layer is even greater than that of the big tank since the free baroclinic layer is very thin. The question is how thin the fluid layer may be before Ekman effects influence baroclinic instability.

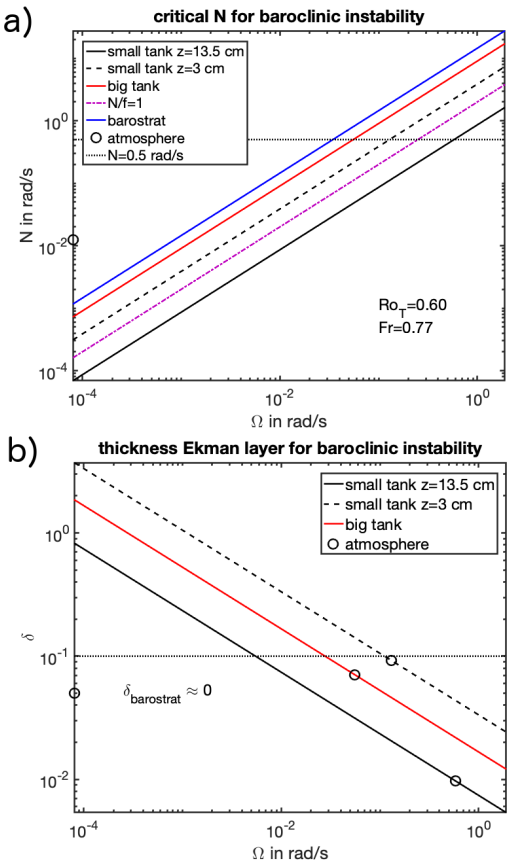

Fig. 1 (a) Critical buoyancy frequency N as a function of the rotation rate Ω calculated with (3) for different experiments and experimental configurations. (b) The ratio of the Ekman layer thickness and the fluid depth, δ, as a function of Ω.

What we can already see from the qualitative analysis of the different experiments is that the greater the inverse aspect ratio Π, the more suitable the experimental configurations are to study IGWs. However, when the fluid depth is decreased in the laboratory experiments, viscous effects at the bottom and, in case of a rigid lid, the top of the tank cannot be neglected. To estimate the importance of friction, we have plotted the ratio of the Ekman layer thickness ($\delta_E = (\nu/f)^{1/2}$ where ν is the coefficient of the kinematic viscosity) and the fluid depth $\delta = \delta_E/H$ as a function of Ω in figure 1(b). The circles display values for $N \approx 0.5$ rad/s corresponding with the intersection of the horizontal dashed line with the sloping lines of the different experiments in figure 1(a). The black line for the small tank (with the fluid depth $d_{small} = 13.5$ cm, mostly used for the experiments) is far below the line $\delta = 1$. For the big tank experiment, we find $\delta \approx 0.1$ that corresponds roughly with the (turbulent) atmosphere. For $h = 3\,\mathrm{cm}$ Ekman layers cover about 10% of the fluid depth. As we will see later, this seems to be the limit for the development of regular baroclinic waves close to the transition point.

As mentioned earlier, the barostrat has no Ekman layer (no rigid bottom boundary for the thin layer close to the surface) and is, therefore, an ideal set-up. It should be noted, however, that even outside the boundary layers the flow in the annulus is "more viscous" than the atmosphere, i.e. its characteristic Reynolds number is much smaller than the atmospheric one.

We can conclude that (apart from the barostrat which is technically more complicated), only the big tank system fulfils the requirement $N/f > 1$ and $\delta \leq 0.1$. Next, we study boundary layer effects on baroclinic instability experimentally to confirm the critical δ.

2.2 Viscous systems: consequences of decreasing the fluid depth

As the fluid depth is decreased (for constant thermal forcing and rotation rate), the ratio of the Ekman layer thickness and the fluid depth becomes greater (as in the case of the small experiment with shallow water where $\delta \approx 0.1$) and, therefore we presume viscosity to have a non-negligible influence on the baroclinic instability mechanism. In these cases, we do not expect the Eady model—which is inviscid—to predict the transition between axisymmetric and wave regime correctly. Hide and Fowlis (1965) investigated the effects of viscosity on the transition between axisymmetric and baroclinic wave regime experimentally. What they found is that two external dimensionless parameters mark this transition: the thermal Rossby number, already introduced in (8), and the Taylor number

$$Ta = \frac{4\Omega^2(b-a)^5}{\nu^2 H}. \tag{4}$$

The experimentally measured transition points from axisymmetric flow to baroclinic waves in a $Ta - Ro_T$ diagram follow an anvil-shaped curve (see regime diagrams, e.g., Hide and Fowlis (1965) and Hide and Mason (1975)). Furthermore, (2) and (4) reveal a dependence on the inverse aspect ratio Π. Hence, for a fixed gap width, the transition to baroclinic waves varies with the fluid depth (Lambert and Snyder, 1966). In order to reproduce the experimental curves, several theoretical studies have extended the solutions of the Eady problem taking into account the effects of viscosity. Barcilon (1964) assumed that the effects of friction at the flat rigid bottom and top lid dominate the effects at the side walls. With this approximation, valid for shallow water fluids, dissipation is introduced only at the Ekman boundary layers at the top and the bottom, and in the fluid bulk the model converges to the Eady solution.

Successively, O'Neil (1969) extended the Barcilon (1964) theory by using a systematic analysis to include the effects of sidewalls on the instability results and to allow for a free surface. Her solution for the neutrally stable modes (equation 6.2 in O'Neil (1969)) is a transcendental equation the terms of which are functions of the Burger number and the Taylor number. The transition curves are qualitatively and quantitatively in excellent agreement with the experimental points found by Hide and Fowlis (1965).

Once the geometry of the experiment, in particular the inverse aspect ratio Π, the wavenumber m, and the parameter $\epsilon_B = \Delta_r T/\Delta_z T$ are fixed, the equation can be solved using the shooting method which gives the neutral stability curves. The validity of the solutions is limited to the cases where $\Pi < 1$. Not many attempts have been made to run experiments with $\Pi < 1$. In most cases, the differentially heated rotating annulus is a table size experiment, and the gap has a width varying from $\mathcal{O}(10\,\mathrm{cm})$ to $\mathcal{O}(1\,\mathrm{cm})$. In our laboratory, the small-tank—a rotating annulus with a gap width $L = 7.5\,\mathrm{cm}$—has been used to investigate the shallow water regime and compare the observed transition from the axisymmetric to the wave regime with the transition predicted by the theoretical model from O'Neil (1969). The technical specifications of the experiment are given in the second column of table 2 (for more details about the experiment see Von Larcher and Egbers (2005)).

The experiments were conducted in the following way: initially, the outer and inner annulus were set to the desired (warm and cold) temperature, and the experiment was allowed to warm up for 1 hour until it reached a constant radial ΔT. Then, rotation was switched on and increased stepwise; at each step, we waited for 20 minutes so that the experiment could settle down to a certain baroclinically unstable state. The flow was monitored with an infrared camera which allowed us to measure at which rotation rate the flow regime passed from "axisymmetric" to "regular wave". The same experiment was repeated systematically decreasing the fluid depth from $d = 8$ to 1 cm.

The Burger number for the first observed wave is plotted with blue circles in figure 2 for the different inverse aspect ratio Π; the fitted black dashed curve is compared with the theoretical inviscid Eady model (straight blue line) and the O'Neil viscous model (red curve). Both theoretical models are plotted for baroclinic instability $m = 3$, which corresponds to the wavenumber observed in the laboratory experiment. It can be seen that the O'Neil curve converges to the Eady model for deeper fluid and deviates from this model when going to shallower water systems, as expected. The experimental points are all situated between the

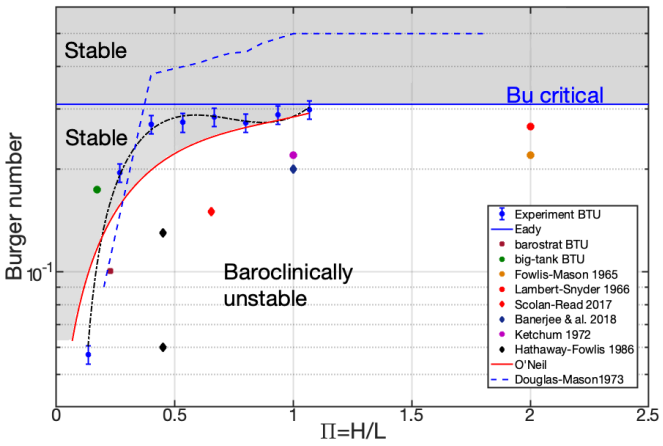

Fig. 2 Plot of the transition from axisymmetric to wave regime for varying fluid depths. The straight blue line shows the (Eady model) inviscid criterium for $m = 3$ and $l = 1$. The red curve shows the transition according to O'Neil (1969) for $m = 3$ to be compared with the black dashed curve which is the fit of the experimental data (blue circles). The error bars show the maximum ΔT variation for different experiments. The grey region is to be intended as stable for $m = 3$ mode, but within it the front can still be unstable with respect to modes with $m < 3$. See text for more details.. For fluid depths $d = 2$ cm and $d = 1$ cm the regime was not regular waves, rather geostrophic turbulence or more irregular waves (see figure 3). The blue dashed curve shows measured data for a rotating annulus with a rigid upper surface from Douglas and Mason (1973). The red and dark yellow dots are points taken from experiments from Lambert and Snyder (1966) and Hide and Fowlis (1965) respectively; note that in both cases the observed wavenumber is $m = 3$ (as for our experiment), but the aspect ratio of their experiment is $\Pi = 2$. The green dot corresponds to the transition observed with the atmosphere-like tank at the BTU. The purple dot corresponds to an experiment done by Ketchum (1972). The diamond-shaped markers are showing data from rotating annulus experiments with a so-called horizontal convection temperature boundary condition (red Scolan and Read (2017), black with $Bu = 0.13$ number for $\Delta T_v = -1$, smaller $Bu = 0.06$ for $\Delta T_v = -1$ see Hathaway and Fowlis (1986), and blue Banerjee et al. (2018)). The squared purple marker shows the transition for the upper layer in the barostrat experiment.

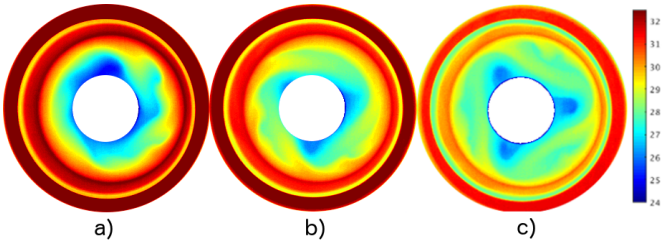

Fig. 3 Snapshots of the flow pattern for the three shallowest fluid depths visualised with the infrared camera (a) $H = 1$ cm, b) $H = 2$ cm, and c) $H = 3$ cm). For $H > 3$ cm the flow regime is a regular wave $m = 3$ similar to the one in (c). The changes in temperature for the different experiments are taken into account with the error bars in figure 2.

two models, except for the shallowest configuration explored (the error bars take into account the small temperature variations for different experiments). Interestingly, for the experiments that were run with water depths $z \geq 3$ cm, we observed a fully developed baroclinic wave, and their points in figure 2 are noticeably closer to the Eady straight line than the two shallowest runs. For these two, having fluid depths of $z = 1$ and 2 cm, a regular wave regime never sets in, and the transition points are marked where we observed the flow to deviate from axisymmetric. For $z = 2$ cm a wavelike instability, confined close to the inner cylinder, was observed (see figure 3(b)), but it did not extend to the full gap width even after waiting for one hour. For $z = 1$ cm, the first regime observed after the axisymmetric one already seems to be turbulent (see figure 3(c)). We increased the rotation rate until $\Omega = 7$ rpm, but could not observe a regular wave. Note that in our analysis we focused on $m = 3$ and we do not know the behaviour for other modes, for example $m = 1, 2$, which are in theory possible but not observed in the experiments we run. However, these modes exist in regimes where the rotation rate is lower than the one for $m = 3$ and hence where the Ekman layer is even thicker. Therefore, we expect a qualitatively similar behaviour as the one shown in 2 for $m = 1, 2$ and that the deviation from the Eady model starts for larger Π. Higher modes might survive for smaller Π.

Our data are further compared with other typical transition points for shallow-water differentially heated rotating annulus experiments present in the literature, plotted in figure 2. The dashed blue curve is taken from Douglas and Mason (1973) and represents the transition for an experimental set-up with a rigid upper boundary. In their work, Douglas and Mason (1973) studied the effect of varying the aspect ratio and compared experiments with the theoretical model by Barcilon (1964), which corresponds to their rigid-lid apparatus. They reported an increase in the azimuthal baroclinic wavenumber measured at the transition point with the decrease of the fluid depth set for the experiment. This might be explained by larger Taylor numbers and smaller Rossby deformation radii for smaller depth. The lid at the upper boundary affects the stability of the flow by shifting the transition of the baroclinic instability to higher Burger number values. Therefore, it has a destabilising effect in agreement with what was observed by Fein (1973) although the upper boundary condition does not substantially alter the baroclinic dynamics. Figure 3(a) shows the possible remains of such a large wave number case in an already turbulent state.

The second set of experiments included in figure 2 are performed in set-ups having a free surface and lat-

eral differentially heating forcing system, performed by Hide and Fowlis (1965) (dark yellow dot in figure 2), Lambert and Snyder (1966) (red dot), and Ketchum (1972) (purple dot). We compare them with the transition for the atmosphere-like tank at the BTU (full details about the transition for this experiment will be given in section 3) marked by the green dot. The first two authors only investigated the region with $\Pi > 1$ for which the theory of O'Neil cannot be applied, while the last author reduced the aspect ratio to $\Pi = 1$. Note that Bu has been re-calculated according to (1), since some authors used different definitions.

The diamond shaped markers show three experimental set-ups for the rotating annulus with different variations of the so-called horizontal convection boundary conditions. The blue data is from Banerjee et al. (2018), for a rotating annulus with a peripheral spot heating system at the bottom on the outer edge and uniform cooling on the inner edge. Another experiment with peripheral local heating at the bottom, but with central cooling by a circular disk placed at the top was proposed by Scolan and Read (2017) and is indicated in figure 2 by the red diamond shaped marker. The last experiment of this kind is a configuration proposed by Hathaway and Fowlis (1986) (black markers) where the radial temperature gradients are imposed on a thermally conducting lid and bottom walls, and the side walls are insulating. The two points are taken from the horizontal difference of temperature $\Delta T_H = 10\,\mathrm{K}$. One with $\Delta T_v = -1$, which gives $Bu = 0.13$, and one with $\Delta T_v = -1$, which gives a smaller $Bu = 0.06$. It seems that in this case, the transition to baroclinic instability occurs for smaller Bu compared to the predictions by Eady and O'Neil for the case of differentially heating at the cylinder walls. These last two mentioned experiments have a similar horizontal scale, each more than one order of magnitude larger than the classical set-up.

Finally, the purple filled square marker indicates the barostrat experiment (Rodda et al., 2018). Although the value of Π for this point corresponds to the one for the "classical" experiment where no fully developed baroclinic wave could be observed (see figure 3(a) and (b)), for the barostrat experiment, a steady wave with $m = 3$ was found. This further confirms that the influence of the bottom Ekman layer inhibits the formation of baroclinic waves. Indeed, the shallow top layer of the barostrat experiment is sandwiched between the free surface and a stably stratified layer; therefore it has no destructive bottom Ekman layer.

In summary, from the results discussed so far we can evince that a tabletop-sized experiment, which is the usual configuration for the differentially heated rotating annulus in laboratories, is unfavourable to study atmosphere-like IGWs. Indeed, these waves require $N/f > 1$ which translate in a demand for $\Pi << 1$; as elucidated by figure 2 and 3 this will result in thin and viscous-dominated layers, which do not allow proper development of baroclinic waves in the classical experimental configuration.

To overcome this problem, one can suppress the Ekman layer, as done in the barostrat experiment by adding a baroclinically stable fluid layer underneath the baroclinically unstable one. The other possible solution is to change the geometry of the experiment by building a system with a large L so that, even for $\Pi << 1$, the fluid depth is still in the order of centimetres and, hence, not dominated by friction.

3 Atmospheric-like new tank—laboratory experiment and numerical simulations

Having discussed why we need a set-up more suitable to study IGWs in the laboratory, we now introduce a new experimental apparatus that was recently built at the BTU Cottbus-Senftenberg laboratory. The set-up of this experiment was introduced in previous numerical studies done by Borchert et al. (2014). Some modifications have been applied to adapt the model's configuration to a feasible laboratory arrangement.

A completely transparent acrylic glass annulus was built and mounted on a rotating table. The annulus is divided into three concentrical gaps by transparent walls, each with a thickness of 1.5 cm (see the picture in figure 4). The middle-gap width measures $L = 35\,\mathrm{cm}$ and the fluid depth is $H = 6\,\mathrm{cm}$, resulting in an aspect ratio $\Pi = 0.17$, which is less than the aspect ratio $\Pi = 0.4$ reached in the small tank with a fluid depth of 3 cm. In the outer gap, warm water is pumped in and out by two pipes positioned diametrically opposite each other. The pipes are fixed to the laboratory frame and connected to an external thermostat that heats the water to the required temperature. A similar system is used to pump cold water into the innermost cylindrical gap. The middle gap is filled beforehand with de-ionised water at the temperature of the lab (kept at a constant 21 °C). When the heating and cooling systems are switched on, the working fluid experiences a difference of temperature in the radial direction due to the heat conduction through the cold inner and the warm outer walls. The rotation of the tank is computer-controlled via a Labview program. While the water temperature in the outer and inner rings is allowed to reach an equilibrium, the rotation of the tank is set to $\Omega = 0.1\,\mathrm{rpm}$. With this system, the pipes stir

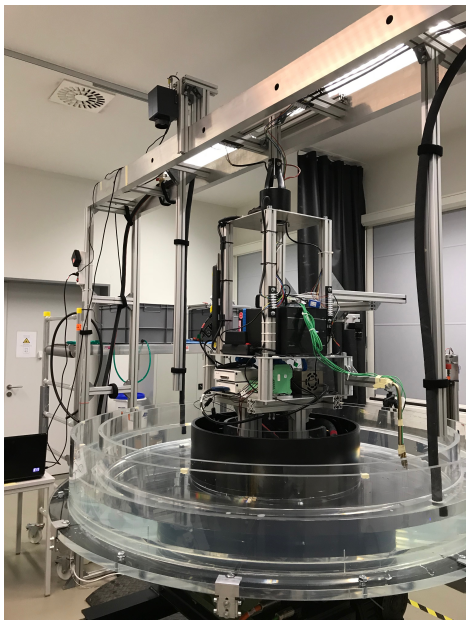

Fig. 4 Picture of the new experimental apparatus.

the water providing an equal distribution of the temperature along the boundary walls. After approximately two hours, a constant radial temperature difference is reached, and we increase the rotation rate (by 0.01 rpm every 15 s) to the final value. The angular velocity range used covers $0.3\,\mathrm{rpm} < \Omega < 1.2\,\mathrm{rpm}$ with an accuracy ± 0.02 rpm, which corresponds to a maximum error of 1.7% for the smallest Ω. The temperature is monitored with sensors placed at the two sides of the walls: in the hot and cold baths, and in the working fluid. The latter is measured at two fluid depths $z = 5\,\mathrm{cm}$ and $z = 1\,\mathrm{cm}$ from the bottom of the tank for the warm and cold wall (see figure 5) with sensors of diameter $d = 1.4\,\mathrm{mm}$. Because the lateral thermal boundary layer thickness is about 0.5 mm (see appendix A), these sensors measure the temperature in the boundary layer or just outside of it. These are used to determine the radial temperature difference $\Delta_r T$, which is usually measured outside the boundary layers (Douglas and Mason, 1973). The value of the externally impressed temperature difference, ΔT which is one of the variables in the definition of the thermal Rossby number (8), is calculated by dividing the difference of temperature measured between the cold and warm baths by a factor, taking into account the heat loss due to the conduction through the walls. Note that, because of the thickness and the low heat conduction of the plexiglass, we have a non-negligible heat loss through the lateral walls and with this experimental set-up it is not possible to impose a large lateral difference of temperature, as done in the numerical simulations by Borchert et al. (2014).

The data presented in the following paragraphs, including the plots, both come from the temperature measured in the fluid gap at mid-radius, using thermocouple sheathed sensors consisting of two wires (NiCr-Ni) from ALMEMO®. These sensors are positioned at mid-gap at different fluid depths z =1.7, 2.6, 3.0, 3.8 and 4.4 cm (see figure 5). The diameter of the sensors is 500 µm, the length of the wire is 10 cm, and their operating temperature range is from -200 to 900 °C with resolution 0.1 °C. A control unit synchronises the sampling interval of the sensors, which we set to $\Delta t = 1\,\mathrm{s}$. An infrared camera (Jenoptik camera module IR-TCM 640, 640×480 pixel resolution) fixed in the laboratory frame with a field of view of a section covering approximately 1/5 of the annular gap measures the temperature at the surface (see figure 5(b)).

The geometry and experimental conditions of the laboratory experiment are transferred to corresponding numerical simulations employing the numerical model cylFloit used by Borchert et al. (2014) and Hien et al. (2018). This model applies a finite volume algorithm to solve the Navier-Stokes equations for a Boussinesq fluid in an annular domain. The resolution of the regular grid in cylindrical coordinates is $N_\theta = 600$ azimuthal, $N_r = 200$ radial, and $N_z = 135$ vertical. The boundary conditions applied at the lateral and bottom walls are no-slip. The boundary condition at the top of the tank, simulating the free surface of the experiment, is the slip condition

$$\left.\frac{\partial u}{\partial z}\right|_{z=d} = \left.\frac{\partial v}{\partial z}\right|_{z=d} = 0, \quad \text{and} \quad w|_{z=d} = 0. \tag{5}$$

Therefore, the top condition in the numerical simulations consists of an “inviscid” lid where the stresses tangential to the surface, surface waves, and the surface tension are neglected. Moreover, the top of the annulus is considered adiabatic; thus the heat transfer between the fluid and overhead ambient air is excluded from the model. The omission of wind stress and evaporative cooling might be a source of discrepancies between the laboratory experiment and the numerical simulations (as discussed later). In order to obtain the best possible comparison between model and laboratory experiment, the simulation strategy is based on the experimental procedures. First, a 2D simulation is run with a constant rotation rate of $\Omega = 0.1$ rpm until a steady state is established. Subsequently, a random disturbance is added to the temperature field before a 3D simulation of the entire annulus configuration is performed. The rotational speed is thereby linearly increased by 0.01 rpm every 15 s until the final speed is reached. Over the entire period, at each integration step, a random disturbance is applied to the inner and outer cylinder

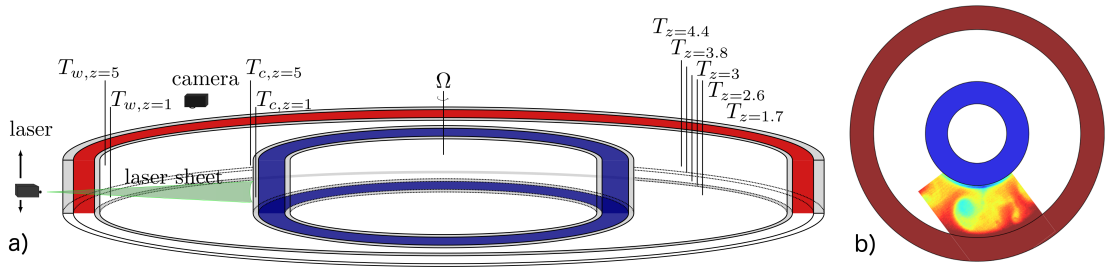

Fig. 5 (a) Sketch of the big-tank geometry and the position of the temperature sensors at the boundary walls (left-hand side) and in the middle of the tank at various fluid depths (right-hand side of the tank). The sensors are positioned along a vertical line. The positions of the co-rotating laser and camera used for the PIV measurement illustrated in section 4 are also shown . (b) Field of view of the infrared camera.

wall temperatures in order to mimic the temperature variations perceived in the experiment.

3.1 Regime diagram

To investigate dominant flow regimes, we run several numerical and laboratory experiments; the imposed temperature difference was kept constant, and we varied the rotation rate. For the imposed temperature difference, the smallest rotation rate for which a baroclinic wave sets in is $\Omega = 0.5$ rpm. A regular wave regime with azimuthal wave numbers varying between $4 \leq m \leq 7$, has been observed for rotation rates $0.5 \leq \Omega \leq 1$ rpm (displayed in figure 6). For $\Omega > 1$ rpm, the flow starts to enter a geostrophic turbulent regime. By running the experiment several times under the same conditions, baroclinic waves with different wave numbers occur, suggesting the existence of multiple equilibria. The numerical simulations confirm these observations.

The minimum and maximum azimuthal wavenumbers observed are consistent with the geometry of the annulus, expressed by the empirical law (Hide and Mason, 1970)

$$\frac{\pi}{4}\frac{b+a}{b-a} \leq m \leq \frac{3\pi}{4}\frac{b+a}{b-a}, \tag{6}$$

which gives $m_{\min} = 3$ and $m_{\max} = 7$ for our experiment. Since $m = 3$ has not been observed, we expect that the region for $m = 3$—for the chosen Burger number Bu and Taylor number Ta—will be small. For other choices of rotation rate and lateral temperature difference, the region for $m = 3$ might be larger and therefore observed in the experiments, but we have not investigated this.

Figure 6 compares the regime diagram for the new atmosphere-like tank with the classical configuration from Vincze et al. (2015) and a large rotating annulus experiment from Scolan and Read (2017), where thermal forcing is applied by local heating and cooling sources. The theoretical instability curves from the O'Neil (1969) model are plotted for both configurations (grey line for the classic, with $m = 3$, and blue for the atmosphere-like rotating annulus, with $m = 4$). The straight red line corresponds to the inviscid instability criterium (1) for $m = 3$. It should be noted that the transitions shown in figure 6 are consistent with O'Neil (1969) and that for both, the small- and big-tank, some baroclinic waves can be observed in the region of the diagram above the inviscid Eady line and below the O'Neil curves. Moreover, these theoretical curves show a very good agreement with the experimental curves from Hide and Mason (1970) (plotted in black in figure 6). Note further that we observed an almost perfect correspondence between the experiments and the simulations with respect to the azimuthal wave numbers (the markers labelled with $m = 0, 4/5, 6/7, 7$ in the regime diagram shown in figure 6 are for both the numerical simulations and the experiment).

The Burger number, Bu, for the classic and the atmosphere-like configuration is calculated by considering the lateral imposed difference of temperature divided by a factor $\sigma_z = 0.3$. Hide (1967) found heuristically that for high Péclet numbers, the parameters $\sigma_z \approx 0.67$ and $\sigma_r \approx 0.33$. These values compare well with several laboratory experiments reported in their paper, which are however all limited to inverse aspect ratio $\Pi > 1$, i.e. tall annuli with narrow gaps and high fluid depths. Experimental studies for $\Pi < 1$ were done by Douglas and Mason (1973) for a differentially heated annulus with rigid upper lid, and they measured a consistent decrease of σ_z and increase of σ_r for decreasing fluid depths. More specifically, for $0.13 < \Pi < 0.2$, which is the range into which our experiment with $\Pi = 0.17$ is included, they measured $0.3 < \sigma_z < 0.5$. We can verify whether this value matches the temperature gradients measured in our atmosphere-like laboratory experiment. First of all, we calculate the Péclet number $Pe = g\alpha\Delta T\nu^{1/2}/8\kappa\Omega^{3/2} = 570$. Since Pe is used to distinguish regimes for which the flow is dominated by thermal conduction (low Pe) to the regimes

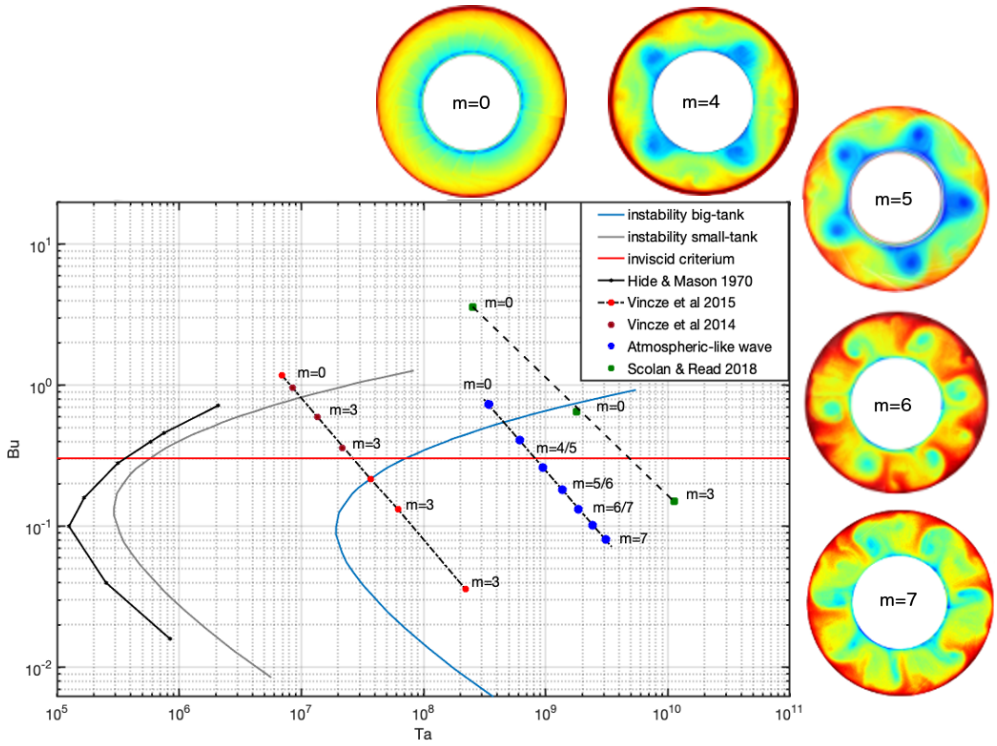

Fig. 6 Regime diagram and instability curves. The straight red line is Eady's inviscid model from (1) for $l = 1, m = 3$, the grey and blue curves are from O'Neil (1969) for the small-tank and the big tank with constant $\epsilon_B = 0.3$ and $m = 3$ and $m = 4$ respectively. The Burger number of the experimental data for the small and big-tank is calculated assuming that $\Delta_z T = \sigma_z \Delta T$ is constant for the different rotation rates, in order to have a better comparison with the model. The small-tank data are taken from Vincze et al. (2015) and Vincze et al. (2014) (darker red dots). The black curve is from experimental data by Hide and Mason (1970). Data from Scolan and Read (2017) are also plotted (green dots) for a comparison with a configuration when Π is < 1. Surface temperature data acquired with an infrared camera show wave flow regimes for different azimuthal wavenumbers found in the new big-tank configuration.

dominated by convection (high Pe), we can see that our experiment falls into the second type of flow. Then, we can calculate σ_z and σ_r and compare them with the values found by Hide (1967) and Douglas and Mason (1973). For an externally imposed $\Delta T = 4.8\,^{\circ}\mathrm{C}$ and $\Omega = 0.7$ rpm, the measured $\Delta_z T$ is in the range $1.7\,^{\circ}\mathrm{C}$ (close to the surface) to $1.3\,^{\circ}\mathrm{C}$ (close to the bottom) giving $\sigma_z = 0.27 - 0.35$. If we, instead, consider the horizontal difference of the vertically averaged temperature measured in the fluid interior (see $\overline{T}_w - \overline{T}_c$ in table 1), the values of the factor raise to $\sigma_r = 0.52 - 0.68$. Our results show excellent agreement with the investigation of Douglas and Mason (1973), confirming a decrease of σ_z and an increase of σ_r for shallow water configurations.

Scolan and Read (2017) measured the stratification through the vertical temperature profiles at mid-radius and used those to calculate the Burger number plotted in figure 6 (green dots). It can be seen that the dashed line connecting the data is not parallel to the other two lines. This shows that the coefficient σ_z is not constant in the parameter regime, but it increases moving towards the bottom right corner in the $Ta - \beta$ diagram.

3.2 Temperature and N

We now compare results from numerical simulations with the experimental data to investigate how well the model developed by Borchert et al. (2014) can reproduce the data in spite of deviations in the upper boundary condition: the omission of surface heat loss due to radiation and evaporation, and the neglection of surface waves and surface tension. As we will see, the deviations are not too significant, and the qualitative structure matches with the experiment. Therefore, we can later use the numerical data to (at least qualitatively) better understand certain features we observe in the experimental data, e.g., the occurrence of gravity waves trapped along the jet axis (Rodda et al., 2018). For this comparison, we select a laboratory experiment and the corresponding numerical simulation, and then investigate the temperature and N field more into detail.

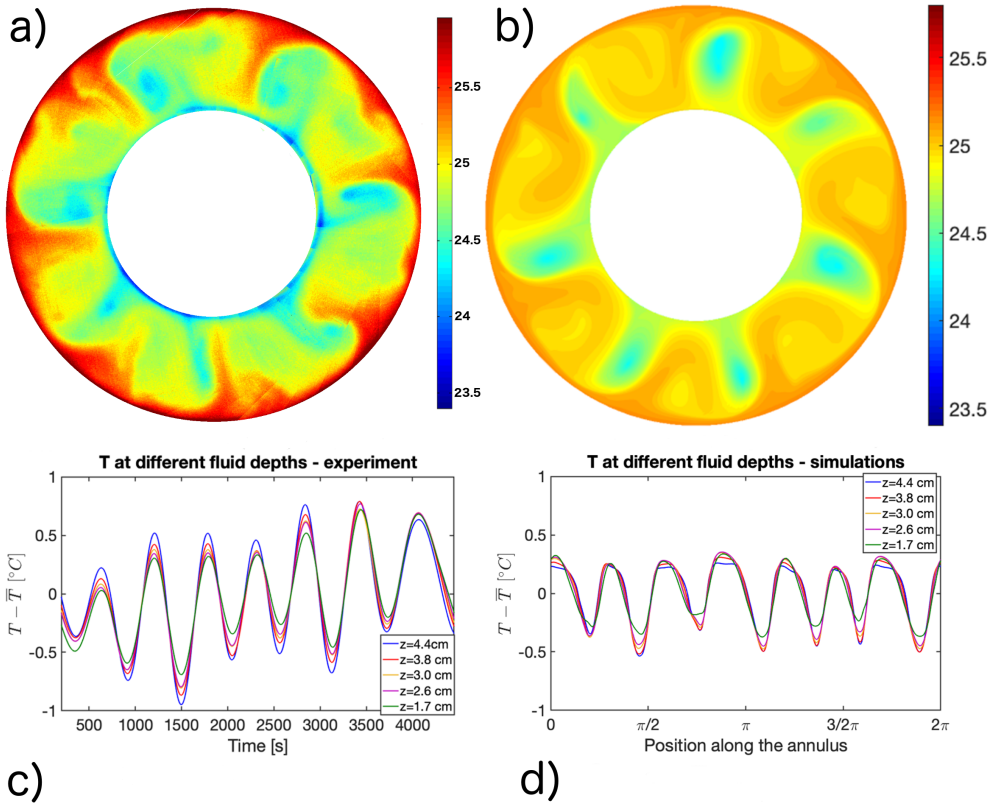

Fig. 7 Surface temperature for the experiment (a) measured with the infrared camera and the numerical simulations (b) plotted for data sampled at the surface, i.e. $z = 6\,\text{cm}$. The mean temperature ($\overline{T}_{\text{laboratory}} = 21.3\,^{\circ}\text{C}$ and $\overline{T}_{\text{simulations}} = 24.2\,^{\circ}\text{C}$) has been subtracted to each time series taken at five fluid depths along a vertical line at mid gap for the laboratory experiment (c) and simulations (d).

For the numerical simulations, the boundary temperature at the walls is constant along the vertical and set to $T_b = 25.6\,^{\circ}\text{C}$ at the outer wall and $T_a = 22.8\,^{\circ}\text{C}$ at the inner wall; a random amplitude noise of $0.5\,^{\circ}\text{C}$ is added to both. For the laboratory experiment the temperature measured by the sensors attached to the walls at two fluid depths $z = 5$ cm and $z = 1$ cm are $T_{w,z=5} = 24\,^{\circ}\text{C}$ and $T_{w,z=1} = 21\,^{\circ}\text{C}$ at the warm wall, and $T_{c,z=5} = 20.2\,^{\circ}\text{C}$ and $T_{c,z=1} = 19.8\,^{\circ}\text{C}$ at the cold wall. From these measurements one can see that the lateral temperature difference closest to the free surface $T_{w,z=5} - T_{c,z=5} = 3.7$ is higher than the one near the bottom of the tank $T_{w,z=1} - T_{c,z=1} = 1.4$. Although the numerical simulations do not capture this depth variation, the mean temperature values close to the boundary lateral walls compare reasonably well, as it can be seen in the second column in table 1.

It is worth mentioning that with N from table 1 and $H = 6\,\text{cm}$ we find $N^2H/g \approx 2.4 \times 10^{-4}$ (for the ocean it is roughly 3×10^{-2}). It is known that for $N^2H/g << 1$ the inertia-gravity wave spectrum is separated from the surface wave spectrum. Accordingly, the surface gravity waves, neglected in the numerical model, will not affect the IGWs (Pedlosky, 2013).

The large-scale temperature patterns at $z = 6\,\text{cm}$ observed in the laboratory experiment and numerical simulation are shown in figure 7(a) and (b). The laboratory experiment temperature is measured with the infrared camera, and the temperature field for the entire annulus is graphically reconstructed combining together subsequently recorded partial images. This can be done because of the symmetry properties of steady waves, which have regular patterns in time. Each image used for the reconstruction is shifted by an angle $\phi = \Omega dt$, where Ω is the rotation of the tank and dt is the time between two recordings. A leading baroclinic wavenumber $m = 7$ is found in both experiment and simulation, after a steady state is reached for the rotation rate $\Omega = 0.7$ rpm. The surface temperature compares qualitatively well in view of the the fact that, in contrast to the experiment, the numerical model has a no flux boundary condition at the upper surface.

The next analysis presented is done by using the temperature data (where the mean value has been sub-

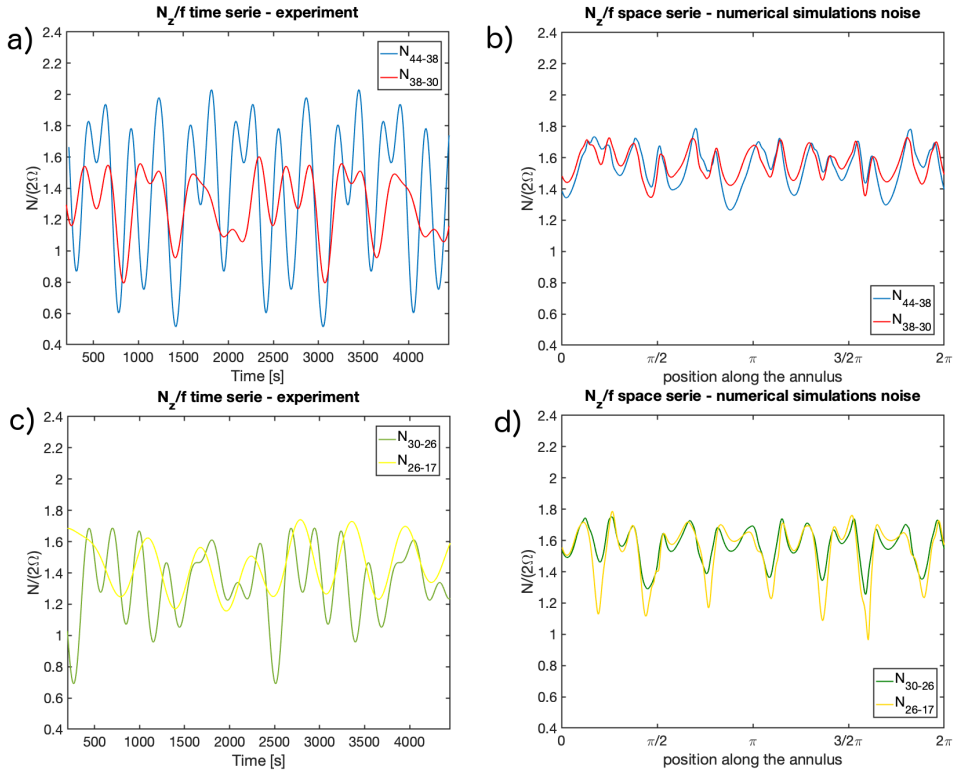

Fig. 8 N/f calculated from the temperature for the two upper most measurements: experiment (a), simulation (b); and the two bottom measurements: experiment (c) and simulation (d).

	f [rad/s]	$\overline{T}_w - \overline{T}_c$[°C]	$\Delta_z T$[°C]	N_H [rad/s]	N [rad/s]	m
Laboratory experiment	0.15	2.5	1.6 -1.5	0.29	0.21 - 0.22	7
Numerical simulations	0.15	2.8	1.5	0.31	0.22	7

Table 1 Comparison laboratory experiment (BTU) and numerical simulations (GUF).

tracted to each of them) taken from five fluid depth points along a vertical line at mid-gap width. The temperature time series for the period that the baroclinic wave needs to travel over the full azimuth from 0 to 2π is shown for the experiment in figure 7(c). This is compared with numerical simulations (figure 7(d)), for which instead of measuring time series at a fixed point, we have taken the data along the entire circumference at mid-gap width at one fixed time. The comparison is made assuming that there is a spatio-temporal equivalence for a steady wave regime. The experimental data show larger amplitude variation with respect to the numerical simulations at all fluid depths. Nevertheless, the vertical temperature differences for the entire water column, calculated as $\Delta_z T = (T_{z=4.4} - T_{z=3.8})H/\Delta z$ (see third column table 1), are consistent. From the measured temperature differences along the radial and vertical directions, we can calculate the buoyancy frequency. $N_H = [(g\alpha\Delta_r T)/H)]^{(1/2)}$ is the buoyancy frequency calculated using the radial difference of temperature measured outside the boundary layers at the walls ($\Delta_r T = \overline{T}_w - \overline{T}_c$, with $\overline{T}$ being the vertical mean between the two measurement points), while $N = [(g\alpha\Delta_z T)/H]^{(1/2)}$ is the buoyancy frequency calculated by using the vertical temperature difference $\Delta_z T$. This gives $N < N_H$ consistent with the previous observation that $\sigma_z < \sigma_r$. Another interesting feature of N is shown in figure 8, where on the left-hand side there are the plots for the laboratory experiment (a) for the two uppermost and (b) for the two bottom most measurements. On the right-hand side are the corresponding plots for the numerical simulations (b) and (d). The mean value for N is the same and it is greater than the Coriolis frequency f. However, the amplitude of the vacillations measured in the experiment is two times that of the oscillations measured in the numerical simulations, particularly when the data close to the water surface are considered (figure 8(a) and (b)). It is likely that these differences at the surface come from the differences of the upper boundary conditions found between simulation and experiment. Note that taking the values from table 1 we see that $N_H/\Omega \approx 4$. This value corresponds

rather well with our estimate from figure 1(a) where we found, for $\Omega = 0.075$, $N/\Omega = 4.5$. The measured value for the vertical temperature gives $N/\Omega \approx 3$, and by taking this, the circles in figure 1(b) for the atmosphere-like tank move towards the value $\delta = 0.1$, indicating that we are close to the critical ratio between the Ekman layer and the total fluid depth with $d = 6\,\mathrm{cm}$, as used in our experiment. Indeed, for experimental runs with a total fluid depth $d = 4\,\mathrm{cm}$, no stable baroclinic waves could be observed. This shows that our conclusion taken in section 2.1 on the basis of simple scaling arguments, saying that only a tank with a small aspect ratio H/L provides a $N/f > 1$, is correct. Together with the experimental finding from section 2.2, namely that $H \geq 3\,\mathrm{cm}$ for steady baroclinic waves in the small tank filled with homogeneous water, we have experimentally shown that a tank with $4\,\mathrm{cm} < H << L$ is better suitable to study atmospheric-like gravity wave emission from baroclinic jets.

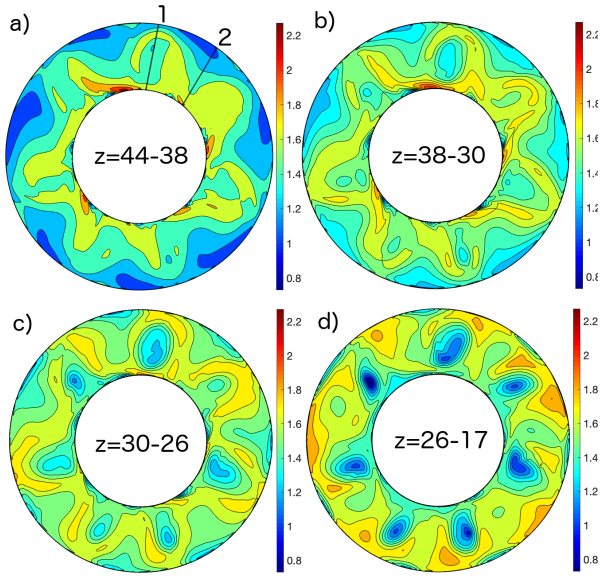

Fig. 9 Horizontal maps of N/f at different fluid depths (see figure 7) from temperature numerical simulations data taken from z =1.7, 2.6, 3.0, 3.8 and 4.4 cm. The lines in (a) labelled with 1 and 2 show the positions along which the vertical profiles of figure 10 are taken.

3.3 Spatial structure of N/f and gravity wave trapping

To better understand the spatial variation of N/f in the annular domain, we plotted horizontal maps in figure 9 using the data from the numerical simulation. A similar pattern can be observed for all the fluid depths considered. More specifically, N has maxima along the baroclinic wave jet. The minima, instead, change position according to the fluid depth. Close to the surface, low values of N/f are visible towards the outer wall, while close to the bottom they appear at the core of the baroclinic wave. We can also notice that $N < f$ in the regions where there is a minimum. This can be relevant for the propagation of atmosphere-like IGWs. Consequently, if gravity waves are spontaneously generated by the baroclinic wave, then they are therefore able to propagate only in regions where $N/f > 1$. In this case, the spatial distribution of N/f shows how the maxima along the baroclinic jet could become a region where IGWs will become trapped. This might be even more accentuated in open surface laboratory experiments, where we have already seen that the oscillations of N/f are larger and therefore, when compared to the simulations, the region for which IGW propagation is permitted could be even more pronounced along the baroclinic wave jet. An example of IGW patterns suggesting wave trapping along the jet has been reported by Rodda et al. (2018) (see their figure 10). In their experiment, the small-scale waves have been observed to propagate mainly due to advection along the baroclinic wavefront, showing characteristics typical of wave capturing (Bühler and McIntyre, 2005). In summary, we found that the baroclinic jet shapes the background buoyancy frequency N. The distribution of N has a large effect on gravity waves ($N > f$) but not on inertial waves ($N < f$).

Finally, we consider vertical-radial planes of the temperature and N/f taken along two radial lines, one in the centre of the baroclinic cyclone and the other in the baroclinic anticyclone (black lines 1 and 2 in figure 9(a)). The mean and the difference are computed and plotted in figure 10(a) and (c), and figure 10(b) and (d) respectively. The temperature shows a maximum variability of 1% in the region where cyclones and anticyclone cores are alternating, assuming lower values in the cyclones. During the cyclone, the isotherms show a positive slope at the inner wall and negative slope at the outer wall, indicating a geostrophic jet at the outer and inner wall. N/f shows a stronger variability close to the upper surface and the bottom, with a larger value of N in the upper region and a smaller value of N in the lower region in the cyclone, and vice-versa in the anticyclone. In the central region of the gap, the variability is zero. This gives a wider IGW frequency band $f < \omega < N$ located in the upper half during the cyclone and near the bottom during the anticyclone. It is important to note that the horizontal maps show, in general, a much stronger total variability for N/f than the one measured in the meridional plane.

Borchert et al. (2014) compared similar plots for the classical configuration (figure 3 small-tank in their paper) and for a larger and shallower water configuration

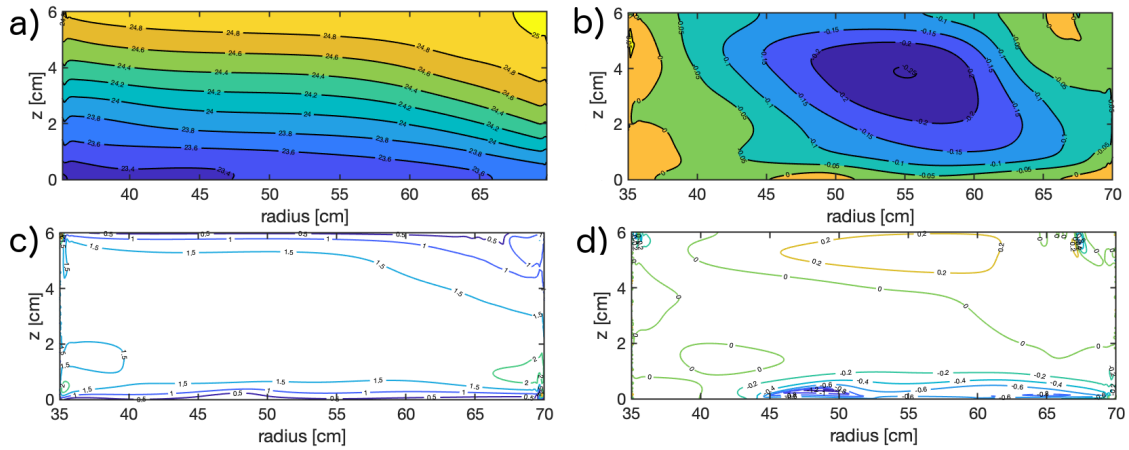

Fig. 10 Vertical-radial plane of numerical simulation data taken along lines 1 (baroclinic cyclone) and 2 (baroclinic anticyclone) in figure 9(a): temperature mean with contour interval 0.2 °C (a), temperature difference with contour interval 0.05 °C (b), N/f mean with contour interval 0.5 (c), and N/f difference with contour interval 0.2 (d).

(figure 5 big-tank, also in their paper). The maximum value of N/f they found for the small tank is equal to 0.5, showing that atmosphere-like IGWs cannot propagate in classical configurations where $\Pi > 1$. When $N < f$ the generation and propagation of IGWs is still possible. Indeed, the values of N and f define the range of the intrinsic frequencies for IGWs, which satisfy the dispersion relation

$$\omega_i = N^2 \cos^2(\alpha) + f^2 \sin^2(\alpha), \tag{7}$$

where α is the angle of phase propagation relative to the horizontal plane. Consequently, for $N < f$ low-frequency waves propagate almost horizontally, while high-frequency waves propagate almost vertically. The opposite is true in the atmosphere, where $N > f$. For this reason, IGWs observed in the classical configuration are expected to behave more similarly to inertial waves rather than gravity waves propagating in the atmosphere.

The profiles by Borchert et al. (2014) for the atmosphere-like tank look qualitatively similar to the ones plotted here in figure 10. Although the imposed lateral difference of temperature in Borchert et al. (2014) is much higher ($\Delta T = 30\,°\mathrm{C}$) than what we used (because of the technical reasons mentioned in section 3), the resulting N/f reaches a maximum value of 4.5 at mid-depth, about two times greater than the maximum value observed here. Except for the top and bottom few millimetres, N/f is always greater than one in the vertical domain. Therefore, atmosphere-like IGW propagation is possible in the entire fluid bulk also for the experimental configuration.

It is finally worth noticing that the isopycnals in figure 10(a) intersect at the top and the bottom. From the experiments done by Scolan et al. (2014) in a similar geometry but with salinity stratification an outcropping region is found for Bu and Ro numbers similar to ours (see figure 11.3 (b) in Scolan et al. (2014)). For the two-layer case, such intersection involves a singular point at the boundary with strong instabilities and possible wave generation which then continue to move along the isopycnals. Further investigations are necessary to verify whether such instabilities can also occur in our experiment where we have a continuous stratification.

4 Gravity waves in the differentially heated rotating annulus with "big-tank" geometry

This last section is devoted to the gravity wave signal observed along the baroclinic jet in the atmosphere-like laboratory experiment. Gravity waves are identified in the horizontal divergence, which is a quantity often used in numerical simulations (O'Sullivan and Dunkerton, 1995) and atmospheric observations (Wu and Zhang, 2004; Dörnbrack et al., 2011; Khaykin et al., 2015) as a dynamical indicator of gravity waves. The horizontal divergence is calculated from the velocity field, which is measured in our experiment via the Particle Image Velocimetry (PIV) technique. This non-intrusive flow measurement consists of tracking the patterns of neutrally buoyant particles, which are spread in the fluid and used as tracers, and then calculate the velocities of the flow. The particles (hollow glass spheres from DANTEC of mean size 10 µm and density 1.1 g cm^{-3}) are illuminated by a diode-pumped steady laser (model Nano 250-532-100 from Linos AG emitting a monochromatic beam at wavelength 532 nm with a power of 100 mW). The laser beam goes through a cylindrical-lens optical system that spreads it into a 2D plane sheet with a

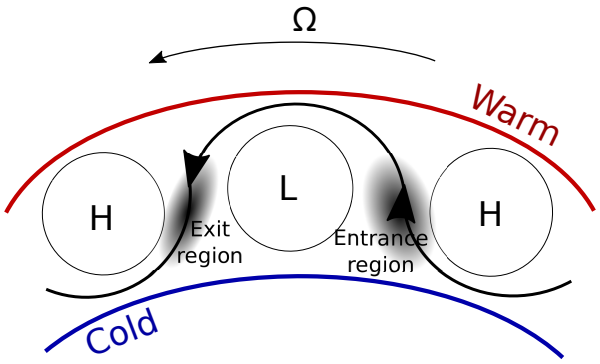

Fig. 11 Sketch of the location for the entrance and exit regions (gray shadows) along the baroclinic jet that form in the differentially heated rotating annulus. A sector of the experiment is represented and the red and blue lines indicated the warm external and cold internal walls respectively. The circles labelled with L and H show the low and high pressure regions around which the jet meanders form.

thickness ≈ 1 mm, which is small enough to be approximated to a two-dimensional plane. A GoPro camera (model hero black modified with lenses TCL1216 from The Imaging Source® and set to video resolution 1080p, which corresponds to a screen resolution of 1920×1080, recording 48 fps) is fixed above the water surface, and records the time evolution of the particles. Both laser and camera are fixed to the tank and co-rotate with it. A sketch with the position of the co-rotating laser and camera system is shown in figure 5(a). The videos recorded are then post-processed with the free Matlab toolbox UVmat[1] and the horizontal velocity components are obtained.

The horizontal divergence maps acquired from the atmosphere-like rotating annulus reveal small-scale features distributed along the baroclinic jet and exhibit a wavelike structure with the wave crests perpendicular to the flow. The manifestation of these small-scale waves along the jet presents many similarities with the observations in the atmosphere that have identified jets and fronts as significant sources of low-frequency inertia-gravity waves. In particular observations, but also numerical models over the years have consistently shown that the jet exit and also the entrance region, although less frequent, are favoured locations for large-amplitude IGWs (see, e.g. Plougonven and Zhang (2014) and references therein, Dörnbrack et al. (2018), and von Storch et al. (2019)). A sketch of the locations for these two regions along the baroclinic jet in the experiment is shown in figure 11.

To show the enhancement of inertia-gravity wave signatures at the entrance and exit of the baroclinic jet, we consider an arc at the mid-radius of the tank and study the temporal evolution along this arc of the radial velocity component and horizontal divergence. Figure 12(a) shows the evolution in time of the spatial mean (calculated along the arc) of the radial velocity component and figure 12(b) the horizontal divergence in a space-time plot, also called Hovmöller plot. In figure 12(a), one can easily notice that three fronts are travelling through our measurement window over time. This happens because the baroclinic wave propagates prograde, and we measure in the co-rotating system. The negative slope corresponds to the exit region of the jet and the positive slope to the entrance of the jet, as indicated in the plot.

The small-scale features can be seen distributed along the oblique lines, the slopes of which have been indicated on the right of the plot by the dashed line. These regions correspond to the baroclinic wavefront, and their slope is the drift speed of the wave itself. Therefore, it can be seen that the small waves are continuously emitted along the jet and propagate with it. A very similar behaviour was already observed for the barostrat experiment (see figure 14 in Rodda et al. (2018)). The small waves do not seem to propagate away from the jet, but they travel trapped within it. This is in agreement with what we discussed in section 3.3, where we speculated about a preferred region for the gravity waves to propagate as a consequence of the horizontal variation of N/f.

A similar analysis has been done by Lovegrove et al. (2000) for small-scale waves observed in the shear-driven version of the baroclinic annulus. Their Hovmöller plot shows many features in common with ours: the small-scales are embedded in the front and propagate faster than the drift speed of the baroclinic wave. This can be deducted by the steeper inclination of the short lines (one is indicated with the solid black line to help visualisation) in figure 12(b), compared to the flatter diagonal ones crossing the whole Howmöller plot (dashed black line) and indicating the typical velocity along the front.

We mentioned in the introduction that spontaneous emission, i.e. the mechanism according to which the evolution of well-balanced flows would lead to the emission of IGWs, is an important generation process at the baroclinic jet. Although the flow is balanced and, therefore, the global Rossby number is small, it can locally grow in localised regions as, for example, the baroclinic fronts and lead to the emission of IGWs. In particular, spontaneous emission is found to be more prominent for $Ro = O(1)$ or larger (Schecter, 2008; Vanneste, 2013). In contrast, a $Ro \ll 1$ regime shows a very weak to nearly negligible emission of gravity waves. For this reason, many studies (see for example, O'Sullivan and

[1] http://servforge.legi.grenoble-inp.fr/projects/soft-uvmat

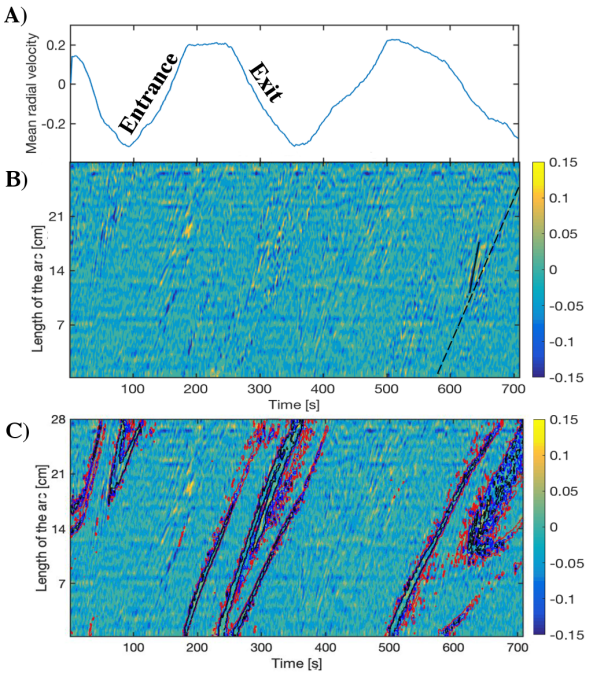

Fig. 12 Mean radial velocity (a), horizontal divergence space-time (Hovmöller) plot (b), and the same as (b) but with the contour lines for the local Rossby number $Ro > 1$ shown in red, $Ro > 1.5$ in blue, and $Ro > 2$ in black (c). The positive slope of the radial velocity correspond to the entrance region of the jet, while the negative slope is the exit of the jet. A stronger signal in plot (b) is visible in correspondence of the entrance and exit region of the baroclinic jet. The dashed line indicates the propagation of the inertia-gravity waves, while the solid black line shows the typical velocity along the front. In plot (c) the dependence of the horizontal divergence on the local Rossby number maxima can be seen.

Dunkerton (1995), Sato and Yoshiki (2008)) have used the Rossby number as an indicator for regions of imbalance in the atmosphere.

Using a similar approach, we can look for a correlation between IGWs and an enhancement of the local Rossby number. In figure 12(c) the Hovmöller plot for the horizontal divergence is shown with superimposed lines that indicate the local Rossby number calculated as:

$$Ro = \frac{\zeta}{f}, \tag{8}$$

where $\zeta = \partial v/\partial x - \partial u/\partial y$ is the vorticity. The red contour lines are for $Ro > 1$, the blue for $Ro > 1.5$, and the black for $Ro > 2$. The regime diagrams of the possible instabilities for the mechanically driven rotating annulus by Gula et al. (2009) and Scolan et al. (2014) show that Rossby-Kelvin instability is possible in the regime of the baroclinic instability and could be responsible for the emission of small-scale waves. Unfortunately, such a diagram is not available for our experiment yet, and a more detailed analysis of the possible generating mechanisms is postponed for following studies. Nevertheless, the correlation between high values of the local Rossby number and high divergence signal is an indicator that spontaneous imbalance could be responsible for the inertia-gravity waves we observe in the experiment. In the future we hope that our experiment will shed more light on the scaling of the wave signal with Ro and Fr. This would be an important step to parametrise IGWs in weather and climate models, an actual topic of the present research.

5 Conclusions

The primary goal of the current study was to discuss the limitations of the classical baroclinic rotating annulus configuration (i.e. tanks having a gap width of the order of centimetres and a homogeneous working fluid) when used to investigate emission and propagation of atmospheric IGWs and to show what changes are needed to provide a more suitable set-up. The new proposed experiment, indeed, led to the observation of inertia-gravity waves along the baroclinic jet that have not been observed in the classical set-up so far. First of all, we have proven experimentally how, for annuli having a gap width of the order of centimetres, it is impossible to reach a low value for the aspect ratio without having to deal with the viscous Ekman layer, which inhibits the formation of a steady baroclinic wave. By increasing the horizontal dimensions of the experiment, we obtained an aspect ratio equal to half the aspect ratio obtained for the classical configuration for the fluid depth $z = 6\,\mathrm{cm}$, which granted the formation of baroclinic waves undisturbed by the bottom viscous Ekman layer. Moreover, by decreasing the aspect ratio, the baroclinic instability regime is reached for higher values of N/f, which is a crucial point for the generation and propagation of IGWs. Consequently, this results in a broader band of intrinsic frequencies for the gravity waves, meaning that we can expect to observe a broader spectrum of propagating and trapped gravity waves in the experiment. The thickness of the Ekman viscous layers at the bottom of the experiment has the same order of magnitude ($\approx 0.5\,\mathrm{cm}$) for both experimental configurations. The thickness of the viscous Stewartson layers at the lateral walls, however, increases one order of magnitude in the wider annulus, reaching the order of a few centimetres. This is something that should be kept in mind in future investigations for spontaneous emission of IGWs since small-scale waves have been reported to be generated at the lateral walls from boundary wall instabilities (Jacoby et al., 2011; Von Larcher

et al., 2018), although they seemed to be trapped at the wall.

Another two aspects that we investigated in detail in our work are the vertical and radial temperature fields, using data recorded in the laboratory experiment and the numerical simulations. In general, even though some discrepancies can be expected because of the approximations made in the numerical simulations for an adiabatic and wind stress-free surface, a good quantitative and qualitative match has been observed between the two. What we observed in the experiment, is that the two temperature gradients along the vertical and horizontal directions do not match. Hide (1967) introduced the factors σ_z and σ_r as a measure of the vertical and horizontal temperature gradient respectively and found that $\sigma_z > \sigma_r$ for the classical configuration. Our studies show instead that this ratio reverses, i.e. $\sigma_z < \sigma_r$ for the atmosphere-like configuration. Furthermore, the two parameters are not constant over the regime diagram and, therefore, the approximation we made in our initial discussion, $Fr \approx Ro_T^{(1/2)}$, must be considered as a first guess only. Since $Bu = \sigma_z Ro_T$, $Fr = (Ro_T/\sigma_z)^{(1/2)}$ follows and because σ_z increases towards the geostrophic turbulence area of the regime diagram, it suggests that for this regime the background conditions come closer to the one considered for Lighthill radiation, since Fr becomes smaller as required. Note that still the wave source, considered to be small compared to the long gravity wave in shallow water, is different for the stratified case. Therefore, caution should be exercised when introducing spontaneous emission into stratified fluids in the context of Lighthill radiation.

The detailed study for horizontal and vertical maps of the buoyancy frequency has shown how atmosphere-like IGWs can, in principle, be generated and propagate over almost the entire fluid domain. However, because of larger variations observed in the laboratory experiment compared to the numerical simulations, we speculate that there are larger regions that are forbidden for the gravity waves to propagate. This is confirmed by the observation of waves trapped along the baroclinic jet, where the buoyancy frequency is observed to reach its maximum value. Plougonven and Snyder (2005) showed with numerical simulations how the wave capture mechanism might be useful to predict the location and several characteristics of spontaneously generated gravity waves. Because captured waves have shorter scales, they can break and therefore become relevant for turbulence and mixing. This, together with the fact that gravity waves with similar characteristics are observed in the atmosphere (Suzuki et al., 2013), calls for further investigation. This again shows that, laboratory experiments could support the numerical simulations offering a realistic background flow without scale dependent approximations. The effect of the upper boundary condition on gravity wave generation and propagation is still undergoing research. A modified experiment with a top lid and numerical simulations with a heat flux at the water surface are planned for the near future.

Acknowledgements C.R. and U.H. thank Ludwig Stapelfeld, Robin Stöbel, Vilko Ruoff for technical support. Moreover, we thank the Spontaneous Imbalance group of MS-GWaves, (Lena Schoon, Christoph Zülicke) for support and fruitful discussions. C.R. and U.H. thank the German Research Foundation (DFG) for the support through the Spontaneous Imbalance project (HA 2932/8-1 and HA 2932/8-2), which is part of the research unit FOR 1898 Multiscale Dynamics of Gravity Waves (MS-GWaves). S.H. and U.A. thank the DFG for partial support through the research unit FOR 1898 MS-GWaves and through grants AC 71/8-1, AC 71/9-1, AC 71/10-1, AC 71/9-2, and AC 71/10-2. The authors are also grateful to the anonymous reviewers for their suggestions that helped to improve the paper.

A Experimental parameters

The thickness of the boundary layers are calculated as: viscous Ekman boudary layer

$$\delta_E = HEk^{\frac{1}{2}}, \tag{9}$$

viscous Stewartson layer at the side walls

$$\delta_s = (b-a)Ek^{\frac{1}{3}}, \tag{10}$$

and the thermal boundary layer at the side walls

$$\delta_T = H\left(\frac{\nu\kappa}{g\alpha\Delta T H^3}\right)^{\frac{1}{4}}, \tag{11}$$

where Ek is the Ekman number

$$Ek = \frac{\nu}{\Omega H^2}. \tag{12}$$

References

Banerjee AK, Bhattacharya A, Balasubramanian S (2018) Experimental study of rotating convection in the presence of bi-directional thermal gradients with localized heating. AIP Advances 8(11):115324

Barcilon V (1964) Role of the Ekman layers in the stability of the symmetric regime obtained in a rotating annulus. Journal of the Atmospheric Sciences 21(3):291–299

Borchert S, Achatz U, Fruman MD (2014) Gravity wave emission in an atmosphere-like configuration of the differentially heated rotating annulus experiment. Journal of Fluid Mechanics 758:287–311

Bühler O, McIntyre ME (2005) Wave capture and wave–vortex duality. Journal of Fluid Mechanics 534:67–95

Dörnbrack A, Pitts M, Poole L, Orsolini Y, Nishii K, Nakamura H (2011) The 2009-2010 arctic stratospheric winter–general evolution, mountain waves and predictability of an operational weather forecast model. Atmospheric Chemistry & Physics Discussions 11(12)

Configuration		classical	atmospheric-like
(a) Geometric dimensions			
Inner radius	a (mm)	45	350
Outer radius	b (mm)	120	700
Gap width	$b-a$ (mm)	75	350
Fluid depth	H (mm)	$10-130$	60
Aspect ratio	Π (mm)	$0.13-1.7$	0.17
(b) Experimental conditions			
Difference of temperature range	ΔT (K)	8	5
Rotation rate range	Ω (rpm)	$0.5-10$	$0.1-1.2$
Rotation rate increment	$\Delta\Omega$ (rpm)	0.5	0.01
Azimuthal wave number	m_{min}	3	4
Azimuthal wave number	m_{max}	7	7
Ekman layer thickness	δ_E (m)	4.5 to 0.9 $\times 10^{-3}$	4.5 to 2.7 $\times 10^{-3}$
Stewartson layer thickness	δ_s (m)	9.5 to 1.7 $\times 10^{-3}$	2.5×10^{-2}
Thermal layer thickness	δ_T (m)	3.1 to 5.8 $\times 10^{-4}$	4.8×10^{-4}
(c) Fluid's physical properties (de-ionised water)			
Density	ρ (kg m^{-3})	998.21	998.21
Kinetic viscosity	ν (m^{2}s^{-1})	1.004×10^{-6}	1.004×10^{-6}
Thermal conductivity	κ (m^{2}s^{-1})	0.143×10^{-6}	0.143×10^{-6}
Expansion coefficient	α (K^{-1})	0.207×10^{-3}	0.207×10^{-3}
Prandtl number	Pr	7	7

Table 2 Geometrical and experimental parameters for the two annulii at the BTU laboratories. The small system has been used in a number of previous studies, e.g. Von Larcher and Egbers (2005), Harlander et al. (2011), Harlander et al. (2012), and Rodda et al. (2018).

Dörnbrack A, Gisinger S, Kaifler N, Portele TC, Bramberger M, Rapp M, Gerding M, Söder J, Žagar N, Jelić D (2018) Gravity waves excited during a minor sudden stratospheric warming. Atmospheric Chemistry and Physics 18(17):12915–12931

Douglas H, Mason P (1973) Thermal convection in a large rotating fluid annulus: some effects of varying the aspect ratio. Journal of the Atmospheric Sciences 30(6):1124–1134

Drazin P (1978) Variations on a theme of Eady. In: Rotating fluids in geophysics, Academic Press, New York, chap 3, pp 139–169

Eady ET (1949) Long waves and cyclone waves. Tellus 1(3):33–52

Fein JS (1973) An experimental study of the effects of the upper boundary condition on the thermal convection in a rotating, differentially heated cylindrical annulus of water. Geophysical & Astrophysical Fluid Dynamics 5(1):213–248

Flór JB, Scolan H, Gula J (2011) Frontal instabilities and waves in a differentially rotating fluid. Journal of Fluid Mechanics 685:532–542

Früh WG, Read P (1997) Wave interactions and the transition to chaos of baroclinic waves in a thermally driven rotating annulus. Philosophical Transactions of the Royal Society of London A: Mathematical, Physical and Engineering Sciences 355(1722):101–153

Gula J, Zeitlin V, Plougonven R (2009) Instabilities of two-layer shallow-water flows with vertical shear in the rotating annulus. Journal of Fluid Mechanics 638:27–47

Harlander U, von Larcher T, Wang Y, Egbers C (2011) PIV- and LDV-measurements of baroclinic wave interactions in a thermally driven rotating annulus. Experiments in fluids 51(1):37–49

Harlander U, Wenzel J, Alexandrov K, Wang Y, Egbers C (2012) Simultaneous piv and thermography measurements of partially blocked flow in a differentially heated rotating annulus. Experiments in fluids 52(4):1077–1087

Hathaway D, Fowlis W (1986) Flow regimes in a shallow rotating cylindrical annulus with temperature gradients imposed on the horizontal boundaries. Journal of Fluid Mechanics 172:401–418

Hide R (1967) Theory of axisymmetric thermal convection in a rotating fluid annulus. The Physics of Fluids 10(1):56–68

Hide R, Fowlis W (1965) Thermal convection in a rotating annulus of liquid: effect of viscosity on the transition between axisymmetric and non-axisymmetric flow regimes. Journal of the Atmospheric Sciences 22(5):541–558

Hide R, Mason P (1970) Baroclinic Waves in a Rotating Fluid Subject to Internal Heating. Philosophical Transactions of the Royal Society of London Series A 268:201–232

Hide R, Mason P (1975) Sloping convection in a rotating fluid. Advances in Physics 24(1):47–100

Hien S, Rolland J, Borchert S, Schoon L, Zülicke C, Achatz U (2018) Spontaneous inertia–gravity wave emission in the differentially heated rotating annulus experiment. Journal of Fluid Mechanics 838:5–41

Jacoby T, Read P, Williams PD, Young R (2011) Generation of inertia–gravity waves in the rotating thermal annulus by a localised boundary layer instability. Geophysical & Astrophysical Fluid Dynamics 105(2-3):161–181

Ketchum CB (1972) An experimental study of baroclinic annulus waves at large Taylor number. Journal of the Atmospheric Sciences 29(4):665–679

Khaykin S, Hauchecorne A, Mzé N, Keckhut P (2015) Seasonal variation of gravity wave activity at midlatitudes from 7 years of cosmic gps and rayleigh lidar temperature observations. Geophysical Research Letters 42(4):1251–1258

Lambert R, Snyder H (1966) Experiments on the effect of horizontal shear and change of aspect ratio on convective flow in a rotating annulus. Journal of Geophysical Research 71(22):5225–5234

Lovegrove A, Read P, Richards C (2000) Generation of inertia-gravity waves in a baroclinically unstable fluid. Quarterly Journal of the Royal Meteorological Society 126(570):3233–3254

O'Neil EJ (1969) The stability of flows in a differentially heated rotating fluid system with rigid bottom and free top. Studies in Applied Mathematics 48(3):227–256

O'Sullivan D, Dunkerton TJ (1995) Generation of inertia–gravity waves in a simulated life cycle of baroclinic instability. Journal of the Atmospheric Sciences 52(21):3695–3716

Pedlosky J (2013) Waves in the ocean and atmosphere: introduction to wave dynamics. Springer Science & Business Media

Plougonven R, Snyder C (2005) Gravity waves excited by jets: Propagation versus generation. Geophysical research letters 32(18)

Plougonven R, Zhang F (2014) Internal gravity waves from atmospheric jets and fronts. Reviews of Geophysics 52(1):33–76

Randriamampianina A, del Arco EC (2015) Inertia–gravity waves in a liquid-filled, differentially heated, rotating annulus. Journal of Fluid Mechanics 782:144–177

Read PL, Pérez EP, Moroz IM, Young RM (2014) In: von Larcher T, Williams P (eds) Modeling Atmospheric and Oceanic Flows: Insights from Laboratory Experiments and Numerical Simulations, vol 205, John Wiley & Sons, chap General circulation of planetary atmospheres: Insights from rotating annulus and related experiments

Rodda C, Borcia I, Le Gal P, Vincze M, Harlander U (2018) Baroclinic, Kelvin and inertia-gravity waves in the barostrat instability experiment. Geophysical & Astrophysical Fluid Dynamics pp 1–32

Sato K, Yoshiki M (2008) Gravity wave generation around the polar vortex in the stratosphere revealed by 3-hourly radiosonde observations at syowa station. Journal of the Atmospheric Sciences 65(12):3719–3735

Schecter DA (2008) The spontaneous imbalance of an atmospheric vortex at high rossby number. Journal of the Atmospheric Sciences 65(8):2498–2521

Scolan H, Read PL (2017) A rotating annulus driven by localized convective forcing: a new atmosphere-like experiment. Experiments in Fluids 58(6):75

Scolan H, Verzicco R, Flór JB (2014) Frontal Instabilities at Density–Shear Interfaces in Rotating Two-Layer Stratified Fluids. Modeling Atmospheric and Oceanic Flows: Insights from Laboratory Experiments and Numerical Simulations 205

von Storch JS, Badin G, Oliver M (2019) The interior energy pathway: Inertia-gravity wave emission by oceanic flows. In: Energy Transfers in Atmosphere and Ocean, Springer, pp 53–85

Sugimoto N, Ishioka K, Ishii K (2008) Parameter sweep experiments on spontaneous gravity wave radiation from unsteady rotational flow in an f-plane shallow water system. Journal of the Atmospheric Sciences 65(1):235–249

Suzuki S, Shiokawa K, Otsuka Y, Kawamura S, Murayama Y (2013) Evidence of gravity wave ducting in the mesopause region from airglow network observations. Geophysical Research Letters 40(3):601–605

Ukaji K, Tamaki K (1989) A comparison of laboratory experiments and numerical simulations of steady baroclinic waves produced in a differentially heated rotating fluid annulus. Journal of the Meteorological Society of Japan Ser II 67(3):359–374

Vanneste J (2013) Balance and spontaneous wave generation in geophysical flows. Annual Review of Fluid Mechanics 45

Vincze M, Harlander U, von Larcher T, Egbers C (2014) An experimental study of regime transitions in a differentially heated baroclinic annulus with flat and sloping bottom topographies. Nonlinear Processes in Geophysics 21:237–250

Vincze M, Borchert S, Achatz U, von Larcher T, Baumann M, Liersch C, Remmler S, Beck T, Alexandrov KD, Egbers C, et al. (2015) Benchmarking in a rotating annulus: a comparative experimental and numerical study of baroclinic wave dynamics. Meteorologische Zeitschrift pp 611–635

Vincze M, Borcia I, Harlander U, Le Gal P (2016) Double-diffusive convection and baroclinic instability in a differentially heated and initially stratified rotating system: the barostrat instability. Fluid Dynamics Research 48(6):061414

Von Larcher T, Egbers C (2005) Experiments on transitions of baroclinic waves in a differentially heated rotating annulus. Nonlinear Processes in Geophysics 12(6):1033–1041

Von Larcher T, Viazzo S, Harlander U, Vincze M, Randriamampianina A (2018) Instabilities and small-scale waves within the Stewartson layers of a thermally driven rotating annulus. Journal of Fluid Mechanics 841:380–407

Williams PD, Haine TW, Read PL (2005) On the generation mechanisms of short-scale unbalanced modes in rotating two-layer flows with vertical shear. Journal of Fluid Mechanics 528:1–22

Williams PD, Haine TW, Read PL (2008) Inertia–gravity waves emitted from balanced flow: Observations, properties, and consequences. Journal of the atmospheric sciences 65(11):3543–3556

Wu DL, Zhang F (2004) A study of mesoscale gravity waves over the north atlantic with satellite observations and a mesoscale model. Journal of Geophysical Research: Atmospheres 109(D22)

Young R, Read P (2013) Data assimilation in the laboratory using a rotating annulus experiment. Quarterly Journal of the Royal Meteorological Society 139(675):1488–1504